AGU PUBLICATIONS

Geochemistry, Geophysics, Geosystems

RESEARCH ARTICLE
10.1002/2014GC005436

Low-frequency earthquakes reveal punctuated slow slip on the deep extent of the Alpine Fault, New Zealand

Calum J. Chamberlain[1], David R. Shelly[2], John Townend[1], and Tim A. Stern[1]

[1]School of Geography, Environment and Earth Sciences, Victoria University of Wellington, Wellington, New Zealand
[2]U.S. Geological Survey, Menlo Park, California, USA

Key Points:
- LFEs occur near the Alpine Fault throughout the 3 year study period
- Regional earthquakes cause short-term increases in LFE activity
- Alpine Fault LFEs exhibit exponential magnitude-frequency scaling

Supporting Information:
- Readme
- Figure S1
- Supporting information Text

Correspondence to:
C. J. Chamberlain,
calum.chamberlain@vuw.ac.nz

Citation:
Chamberlain, C. J., D. R. Shelly, J. Townend, and T. A. Stern (2014), Low-frequency earthquakes reveal punctuated slow slip on the deep extent of the Alpine Fault, New Zealand, *Geochem. Geophys. Geosyst.*, *15*, doi:10.1002/2014GC005436.

Received 29 MAY 2014
Accepted 29 JUN 2014
Accepted article online 2 JUL 2014

Abstract We present the first evidence of low-frequency earthquakes (LFEs) associated with the deep extension of the transpressional Alpine Fault beneath the central Southern Alps of New Zealand. Our database comprises a temporally continuous 36 month-long catalog of 8760 LFEs within 14 families. To generate this catalog, we first identify 14 primary template LFEs within known periods of seismic tremor and use these templates to detect similar events in an iterative stacking and cross-correlation routine. The hypocentres of 12 of the 14 LFE families lie within 10 km of the inferred location of the Alpine Fault at depths of approximately 20–30 km, in a zone of high P-wave attenuation, low P-wave speeds, and high seismic reflectivity. The LFE catalog consists of persistent, discrete events punctuated by swarm-like bursts of activity associated with previously and newly identified tremor periods. The magnitudes of the LFEs range between M_L – 0.8 and M_L 1.8, with an average of M_L 0.5. We find that the frequency-magnitude distribution of the LFE catalog both as a whole and within individual families is not consistent with a power law, but that individual families' frequency-amplitude distributions approximate an exponential relationship, suggestive of a characteristic length-scale of failure. We interpret this LFE activity to represent quasi-continuous slip on the deep extent of the Alpine Fault, with LFEs highlighting asperities within an otherwise steadily creeping region of the fault.

1. Introduction

The original recognition of nonvolcanic tremor in southwest Japan [*Obara*, 2002], and subsequent studies in several locations worldwide [e.g., *Rogers and Dragert*, 2003; *Nadeau and Dolenc*, 2005; *Wech et al*., 2012] have revealed seismic deformation occurring under temperature and pressure (depth) conditions previously thought to preclude seismogenesis. Tremor has previously been demonstrated to be a superposition of multiple low-frequency earthquakes (LFEs) in a swarm-like manner [*Shelly et al*., 2007; *Ide et al*., 2007]. The spatiotemporal persistence of LFEs and tremor [e.g., *Rogers and Dragert*, 2003; *Frank et al*., 2013] and their response to small stresses [*Peng et al*., 2009; *Thomas et al*., 2009; *Fry et al*., 2011] provide a means of examining the state of stress at depth and mechanisms of stress transfer from the deep crustal roots of faults to their shallow seismogenic zones [*Wech and Creager*, 2011].

The constituent LFEs of tremor bursts have occasionally distinct, often emergent, P and S phases. Waveform cross-correlation techniques [e.g., *Ide et al*., 2007; *Shelly et al*., 2007; *Brown et al*., 2008, 2013] for identification of repeating LFEs provide a means of detecting multiple similar events. These similar events can then be stacked to improve signal-to-noise ratios (SNRs). Picking both P and S phases of these stacked LFEs allows LFE families to be located more accurately than the tremor signals themselves. Tremor is often otherwise located by cross-correlating a long (2–5 min) waveform packet [e.g., *Wech and Creager*, 2008]. Not only does locating the constituent LFEs of tremor allow for more robust hypocentre locations, but it also allows for tremor fronts to be tracked in high spatiotemporal definition by identifying individual LFE family activity during tremor [e.g., *Shelly*, 2010]. Emergent phase arrivals of LFEs have also been shown to provide sufficient constraints for the calculation of LFE focal mechanisms [*Ide et al*., 2007; *Bostock et al*., 2012; *Royer and Bostock*, 2013].

Tremor has been documented at both subduction and strike-slip plate boundaries, including the transpressive Alpine Fault in South Island, New Zealand. Using data recorded by the Southern Alps Microearthquake Borehole Array (SAMBA) [*Boese et al*., 2012], *Wech et al*. [2012, 2013] documented tremor occurring south of Mt. Cook and attributed this phenomenon to deep slow slip on the Alpine Fault. However, due to large

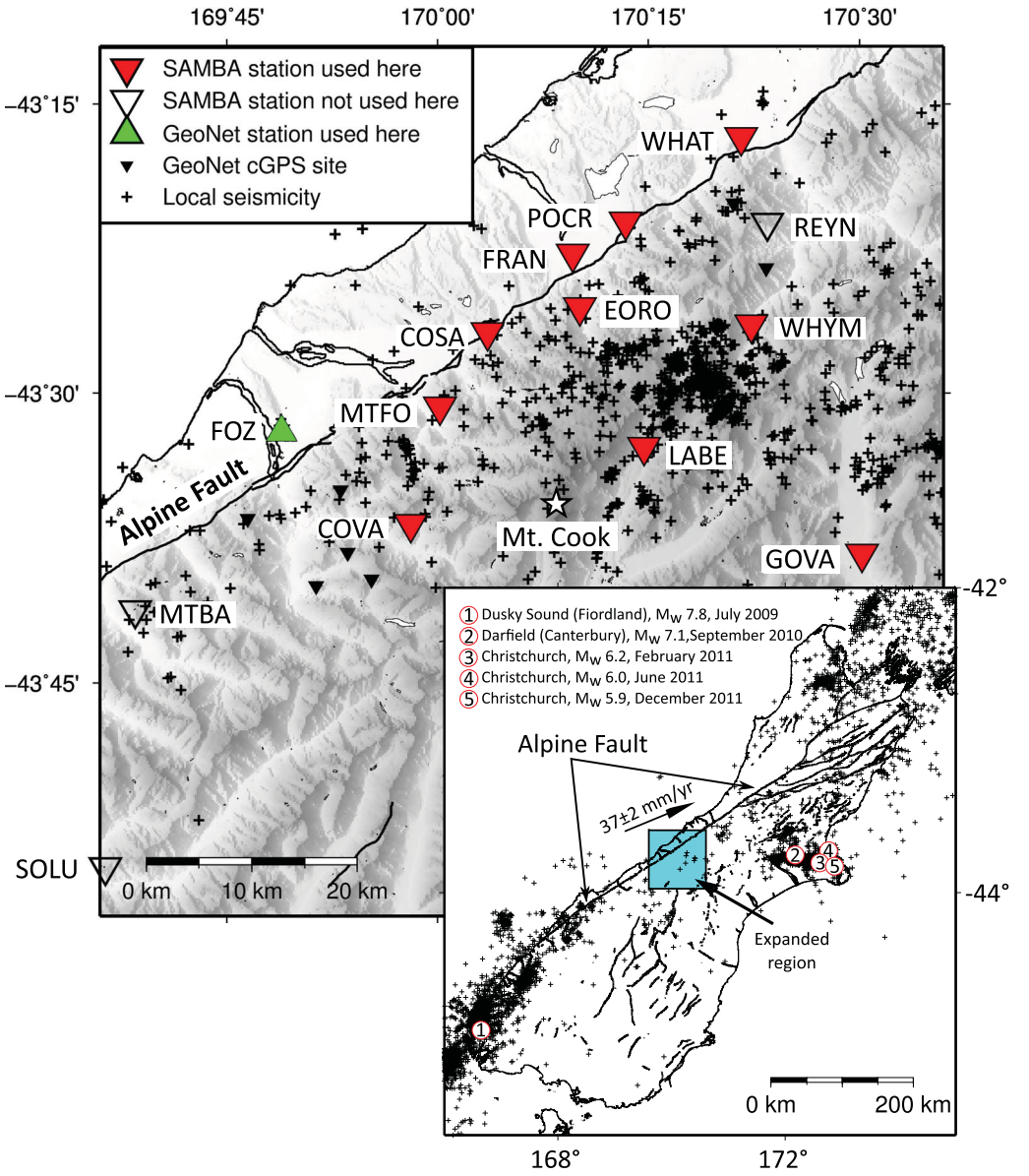

Figure 1. SAMBA network used in this study to detect LFEs with background microseismicity of *Boese et al.* [2012] plotted as black crosses. The two southernmost SAMBA stations (MTBA and SOLU) were not active during the period analyzed but may provide future constraints on LFEs south of the current LFE family hypocentres. Inset: Tectonic setting of South Island New Zealand, with earthquakes seen to trigger increased LFE generation indicated by numbered circles. Background seismicity $M_W \geq 3.0$ from the Geonet catalog for the period 26 March 2009–2 April 2012 plotted as black crosses.

depth uncertainties, ambiguity remains over the relationship of the tremor to the Alpine Fault, with the possibility that tremor occurs not only on the deep extent of the Alpine Fault but also on the northern extent of the subducted Australian plate [*Sutherland et al.*, 2006; *Cox and Sutherland*, 2007; *Boese et al.*, 2013] or on other undocumented structures at depth. This ambiguity may be overcome using refined source locations, made possible through accurate hypocentre locations of LFEs embedded within the tremor.

The Alpine Fault is a transpressive margin of dextral-reverse sense at the boundary of the Australian and Pacific Plates (Figure 1). Geological investigations [e.g., *Norris and Cooper*, 2000; *Sutherland et al.*, 2006] find a C. 23 mm/yr long-term fault-parallel Quaternary slip rate, approximately half the contemporary fault-parallel component of Australia-Pacific motion of 35–40 mm/yr [*Beavan et al.*, 2002]. Uplift rates on the Alpine Fault are greatest (5–8 mm/yr [*Beavan et al.*, 2002; *Houlié and Stern*, 2012]) in the area of highest topographic relief surrounding the Mt. Cook massif [*Little et al.*, 2007].

Table 1. Locations of LFE Families[a]

Family ID	Latitude	Longitude	Depth	Mean M_L	Detections
55115	−43.67	169.91	25 ± 2	0.3	419
55200	−43.56	169.93	27 ± 3	0.3	258
55432	−43.64	170.06	25 ± 3	0.4	486
61100	−43.64	169.93	24 ± 2	0.4	362
30441	−43.68	170.14	27 ± 2	0.4	426
60905	−43.64	170.00	21 ± 3	0.3	308
61044	−43.77	169.98	22 ± 3	0.9	1726
61220	−43.71	170.02	20^{+3}_{-4}	0.5	346
37575	−43.67	170.01	23 ± 2	0.4	1456
63877	−43.67	169.94	26^{+5}_{-3}	0.4	269
59966	−43.67	169.98	23 ± 3	0.4	372
60070	−43.64	170.00	18^{+2}_{-3}	0.3	324
54905	−43.71	170.04	20^{+3}_{-5}	0.5	509
17208	−43.52	170.06	28 ± 2	0.4	577

[a]Mean M_L values for each LFE family. Overall mean M_L for all detected events is 0.5 over the 8760 cataloged events.

Despite high deformation rates, seismicity rates for moderate magnitude (M_w 3–5) earthquakes are lower around Mt. Cook than on the northern extent of the Alpine Fault or the Fiordland Seismic Zone. Seismicity in the central Southern Alps is concentrated in areas of high resistivity gradients [*Boese et al*., 2012]. *Boese et al*. [2012] suggested that outside the seismically active shallow regions, the material is either too hot, too fluid-saturated, or too weak to produce detectable seismicity.

The well-documented quasiperiodic record of ground-breaking Alpine Fault earthquakes with a mean recurrence interval of C. 330 years [*Berryman et al*., 2012] and the inferred year of the last great earthquake on the Alpine Fault (1717 ± 5 C.E.) [*Sutherland et al*., 2007] suggest that the Alpine Fault is late in its average seismic cycle of M_w 7–8 earthquakes, and as such poses substantial hazard to southern New Zealand [*Sutherland et al*., 2012]. By studying LFEs, we may gain some understanding of how stress transfer on the deep extent of the Alpine Fault behaves prior to a major earthquake.

Here we provide the first documentation of LFEs occurring beneath the Southern Alps. Using manually identified LFE templates and the match-filter detection technique employed by *Shelly et al*. [2007], we detect similar LFEs within known tremor periods and throughout the 36 month seismic record of 26 March 2009–2 April 2012. We analyze the interevent times and frequency-magnitude characteristics of the resulting LFE catalog and demonstrate a near-constant background rate of LFE generation punctuated by distinct rate increases on scales of minutes to hours corresponding with tremor, and of days to weeks following large ($M_w \geq 5.9$) regional earthquakes.

2. Methodology

2.1. LFE Identification and Detection

In this study, LFE candidates are first identified by manual inspection of tremor waveforms detected by *Wech et al*. [2012]. We recognize LFEs by their distinctive earthquake-like, near-impulsive arrivals within otherwise emergent tremor waveforms. We require an LFE to have been recorded on at least five stations in order to undergo further analysis. All candidates considered here have S-picks (estimates of S-wave arrival times) at all stations used. The frequency content of LFE candidates is then checked to confirm their difference from "typical" earthquakes: as in other studies [e.g., *Shelly et al*., 2007], our LFEs have peak SNR at frequencies of 2–8 Hz.

We compute preliminary locations using the 1D velocity model described by *Boese et al*. [2012] (modified after *O'Keefe* [2008]) and used subsequently by *Boese et al*. [2013] to locate deep seismicity in the region. We compute hypocentre locations and uncertainties for all candidate events using the Gaussian analytic method in *NonLinLoc* [*Lomax et al*., 2000] and model parameters calculated by *Boese et al*. [2012] for local seismicity, namely a typical model error of 0.075 s in traveltime residuals, a correlation length of 8.0 km (equal to the average station spacing). This method does not include uncertainties in the velocity model which may be large here. As such, hypocentral uncertainties shown here should be considered minimum uncertainties. We do not recalculate velocity model errors as we do not have enough hypocentres within

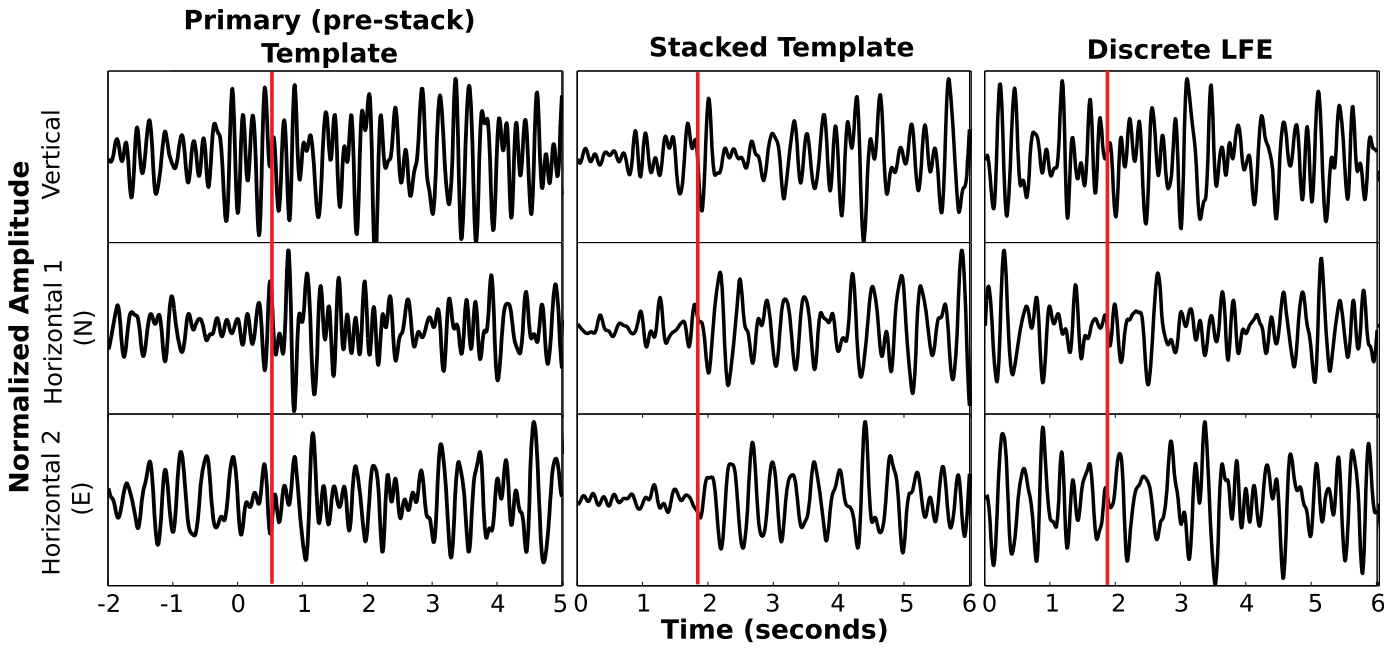

Figure 2. S-wave window for a LFE detected on the SAMBA network and plotted here on all three components of SAMBA station LABE. Times are relative to the start of the window used in correlation for detection of similar events, this begins between 0.5 and 1 s before the S-arrival (red line). From left to right are plotted the primary (prestack) template; the same template after a stack of approximately 1000 waveforms (middle); and a final detection of a discrete (outside of tremor) M_L 0.5 LFE (right). Note that the primary template is padded by 2 s prior to the beginning of the search window to highlight the change from background noise to LFE. A second LFE with S-arrival between 5 and 6 s is also cut from this plot but included in the primary template. All plots are band passed 2–8 Hz as this frequency band contains the highest amplitudes above background noise for our LFE detections. The red line marks the S-phase arrival in all plots. SNR improves after stacking, allowing for more accurate phase picks of both S and P (not shown here as P arrivals are not correlated for at any stage in our method). Note the change in S-pick before and after stacking. This is likely due to noise in the initial manually detected primary template (left) obscuring the true phase arrival and highlights the importance of stacking before locating LFEs.

our dataset. As noted by *Wech et al*. [2012] for the tremor signals within which these LFEs are detected, depths are anticorrelated to both deep (∼ 50–100 km) [*Boese et al*., 2013] and shallow (0–12 km) seismicity [*Boese et al*., 2012].

Once LFE candidates are confirmed, they are then used as primary templates in the detection of similar events by correlation. We scan with fourteen primary template LFEs (Table 1) through the SAMBA waveforms recorded between 26 March 2009 and 2 April 2012. To construct templates, we use a 6 s long window beginning approximately 0.5 s before the S-pick to ensure that we span both the S-phase arrival and its coda for each channel at each station (Figure 2). Templates are correlated on all three channels at each station, yielding a minimum of 15 channels per template upon which detection is based. We do not correlate P arrivals as these are less evident at most stations than the S arrivals for our primary template LFEs.

In constructing the primary templates, we impose an implicit a priori constraint on LFE hypocentre locations by incorporating station-specific delay times. Delay terms are required to cope with large ranges in source-receiver distances throughout the network (4–60 km epicentrally), which in some cases exceed the 6 s template window length. We have found longer windows to increase the risk of correlations being dominated by non-LFE-derived noise and also increase the risk of cycle-skipping when LFEs occur close together in time.

To detect similar events, we cross correlate each of the primary templates through the dataset at 0.01 s intervals. Both the template and dataset are band passed at 2–8 Hz. We detect new LFEs when the network correlation sum exceeds a threshold based on the Mean Absolute Deviation (MAD) value, a statistic that is robust to outliers expected to arise from real event detections [*Shelly et al*., 2007]. We set our detection threshold at 8 times MAD based on synthetic testing outlined in section 2.3. Detections for a single template are constrained to have an 8 s gap between them to reduce the risk of cycle skipping.

Following an initial detection run, we then stack the best 10% of primary detections to generate a higher-SNR secondary template (Figure 2) in a similar fashion to the iterative stacking and cross-correlation routine

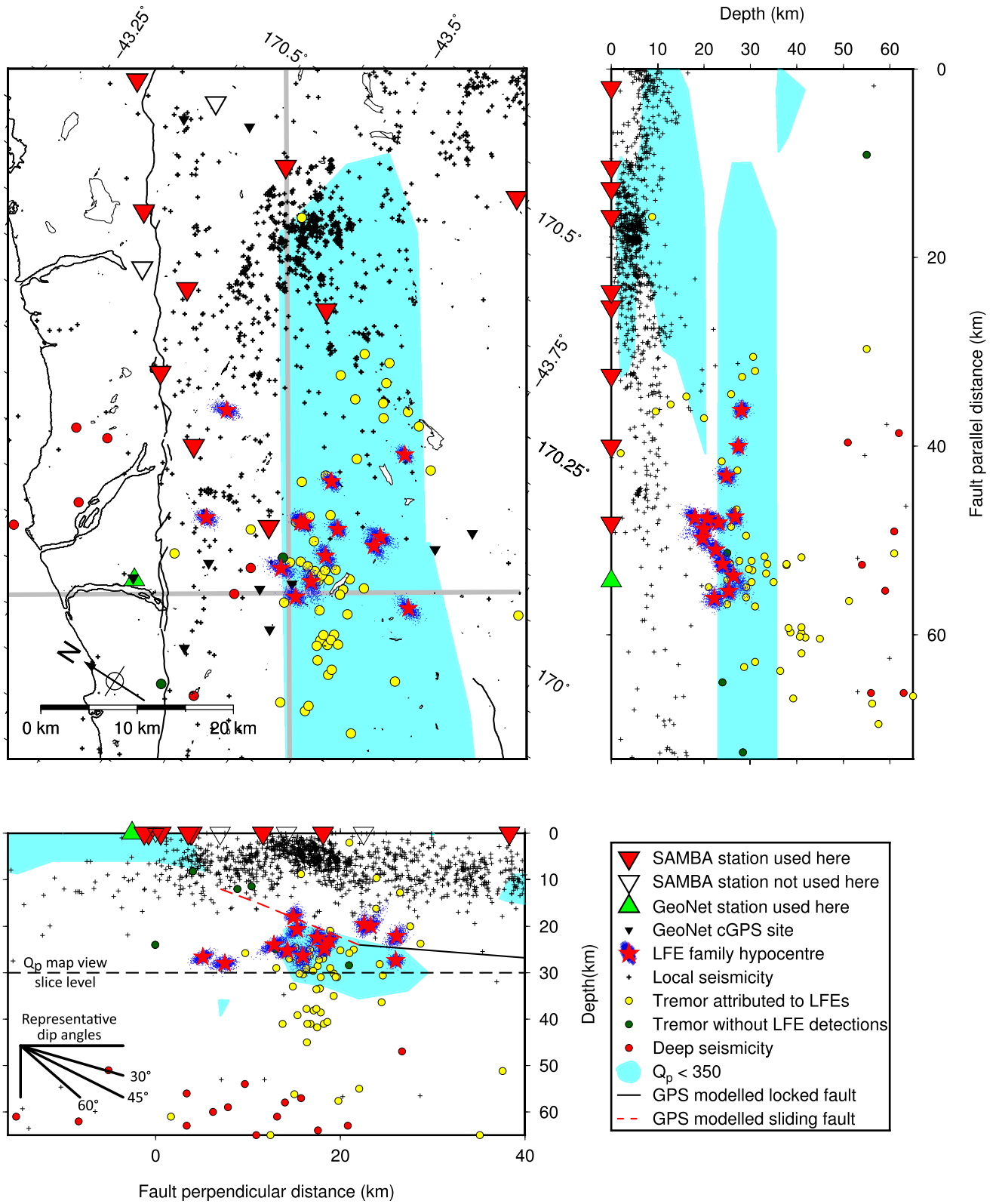

Figure 3. Hypocentre locations of 14 LFE families identified in this study, with uncertainties plotted as blue cloud of probability density function. Local seismicity [*Boese et al.*, 2012, 2014], deep seismicity [*Boese et al.*, 2013], and previously identified tremor [*Wech et al.*, 2012, 2013] are plotted as in the legend. Cross sections projected onto gray lines in map view. GPS modeled fault shown on lower cross section after *Lamb and Smith* [2013]. Low Q_p region (at 30 km depth in map plot as shown by dashed line in fault perpendicular cross section) shaded in cyan after *Eberhart-Phillips et al.* [2008]. All colored triangles indicate stations on which LFEs have been detected. Note the vertical contraction in both cross sections.

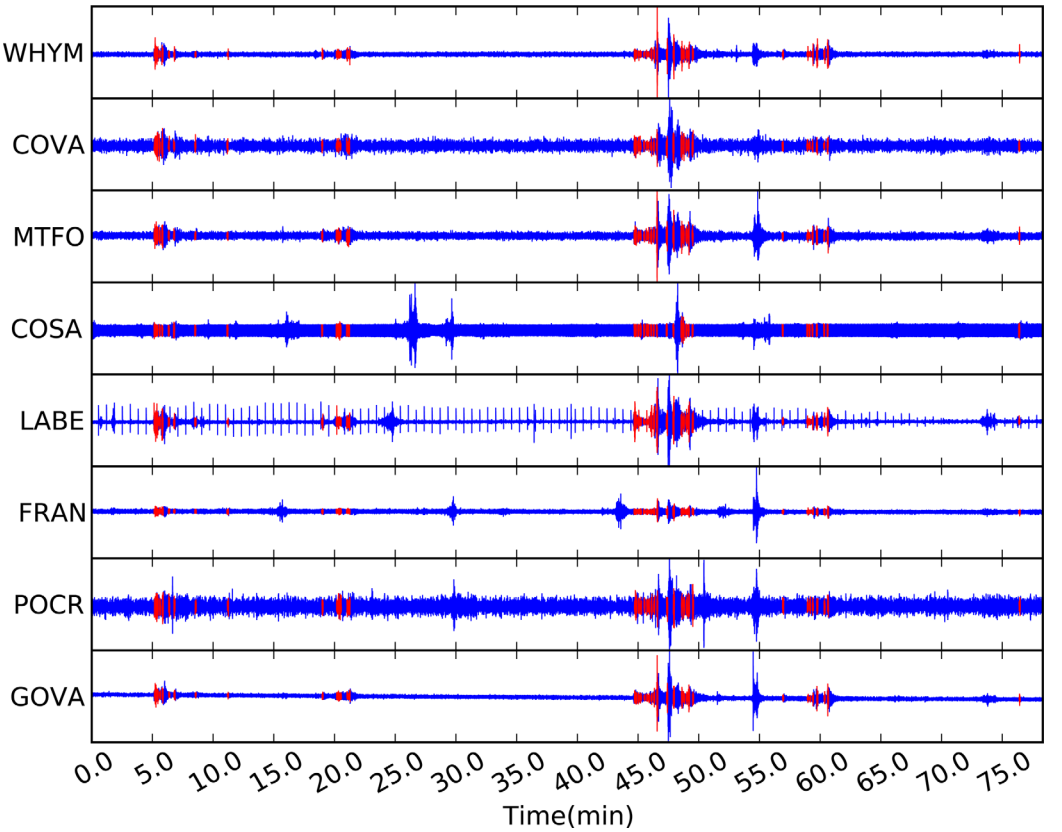

Figure 4. LFE detections (red) within tremor identified by [*Wech et al*., 2012] on eight SAMBA stations. Plot start time is 20 August 2010, 04:41:40.00 UTC. Amplitudes are normalized and data band passed 2–8 Hz. Tremor is discontinuous within the plot window, with the main tremor burst highlighted by [*Wech et al*., 2012] between 43 and 50 min in this plot containing many LFE detections. Obvious spikes in time series recorded on LABE are due to solar-controller defects, the effect of these spikes is discussed in the text.

of *Shelly and Hardebeck* [2010]. During stacking, the template length is extended to 15 s to include both P and S arrivals. At this stage, the stacked waveforms are retained for location analysis. After stacking, P phases often become clearer, in some cases allowing for hypocentre refinement using more phase picks than we are able to achieve with the corresponding primary templates. The secondary template is then recut to 6 s surrounding the S arrival and used in a further cross-correlation detection routine.

In general, the process of iteratively stacking and cross correlating increases the number of detections. We repeat this iterative routine until there is less than a 10% change in detections (either greater or fewer detections), or until the fifth iteration. Once the final stack has been generated, we reevaluate the P and S picks and recompute the hypocentre locations (Figure 3). All final templates are located with P-picks at two or more stations and S-picks at every station.

Some SAMBA stations have encountered problems with noise introduced by solar controllers (LABE, Figure 4) [*Boese et al*., 2012; *Boese*, 2012]. Although the correlation detection routine does not initially detect this noise, any spikes present within a detection will be incorporated in the following, stacked, template. This results in the next correlation routine correlating the spike rather than the LFE. To combat this, we have manually scanned each record and removed channels for time periods showing spiking ($<$ 6 months data removed at each of LABE and POCR). As we require at least five stations for a detection, weaker templates with initial picks on only five station do exhibit fewer detections when we have data loss. Despiking routines were not used as they were found to reduce initial detections and introduced other noise into the stacked templates.

2.2. Magnitude Calculation

For each detected event at each station and channel, we band pass at 2–8 Hz the 6 s window in which the detection was made. We then remove the instrument response to estimate ground velocity and find the

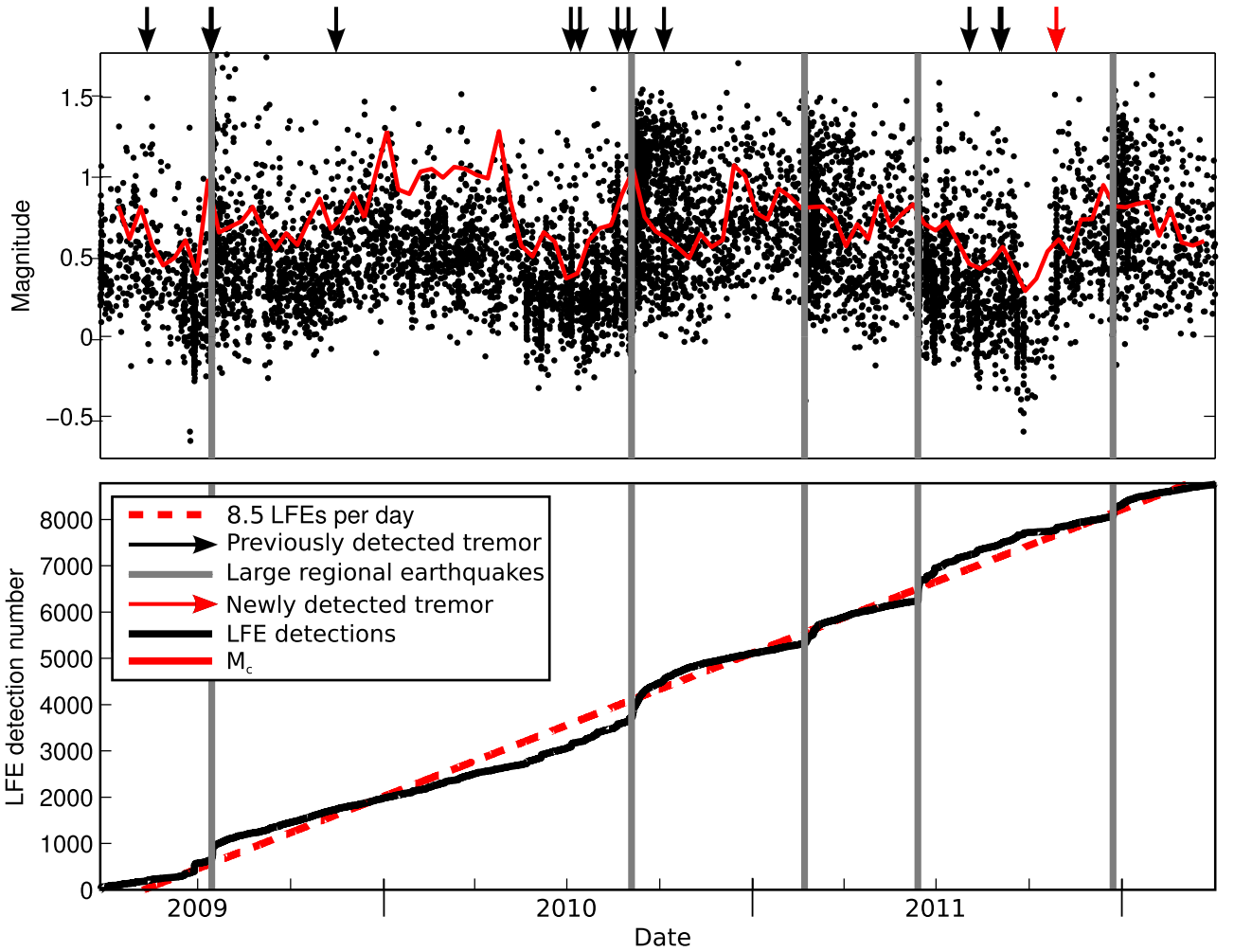

Figure 5. (bottom) LFE detection rates and (top) magnitudes with time. Magnitude of completeness variations with time (10 day running average) plotted as a red line in the top plot. The apparent gap in detections between September and October 2011 is due to data corruption due to spikes as discussed in the text. Gray bars indicate the date of certain major regional earthquakes as discussed in the text (section 4.2). Black arrows indicate tremor periods identified by *Wech et al.* [2012]. A simple linear fit corresponding to 8.5 LFE detections per day is plotted as a red-dashed line. We identify a possible new tremor period outside of the time period analyzed by *Wech et al.* [2012] as a spike in LFE generation (highlighted by a red arrow); this has been confirmed as tremor by applying standard tremor waveform envelope cross correlation techniques and observing similar tremor locations to the LFE source region. We also see rate increases after the regional events indicated here, suggesting LFE and tremor triggering or modulation: tremor was active both before and after the Dusky Sound M_w 7.8 [*Beavan et al.*, 2010] (15 July 2009) earthquake.

minimum and maximum amplitudes and the time between them to give the peak ground velocity (PGV) and frequency. The peak-to-trough velocity amplitude is then converted to a Wood-Anderson amplitude at the specific frequency determined. Band passing and using a single amplitude at a single frequency mitigates the effects of low-frequency amplification of microseismic noise when simulating Wood-Anderson responses for an unfiltered time series [*Havskov and Ottemöller*, 2010]. This amplitude is finally converted to M_L using the coefficients derived for local earthquakes by *Boese et al.* [2012] recorded with SAMBA. We found this routine to give magnitudes within ± 0.2 of the published magnitudes of local seismicity [*Boese et al.*, 2012]. For template LFE events, the automated routine gives the same amplitudes and magnitudes as manual picking.

We remove spuriously large and small single-channel magnitudes ($M_L > 2.0, M_L < -4.0$), which often correspond, respectively, to detections within the coda of large earthquakes or periods of solar controller-induced spiking [*Boese*, 2012], and magnitudes determined on the vertical component. We are always left with more than three magnitude estimates for each event (average 16 channels used). A final event magnitude is given by the mean of all single-channel magnitude estimates for each event. Single-event PGVs are given by the median of the single-channel PGVs for that event. We do not attempt to correct for source-station distance in this calculation.

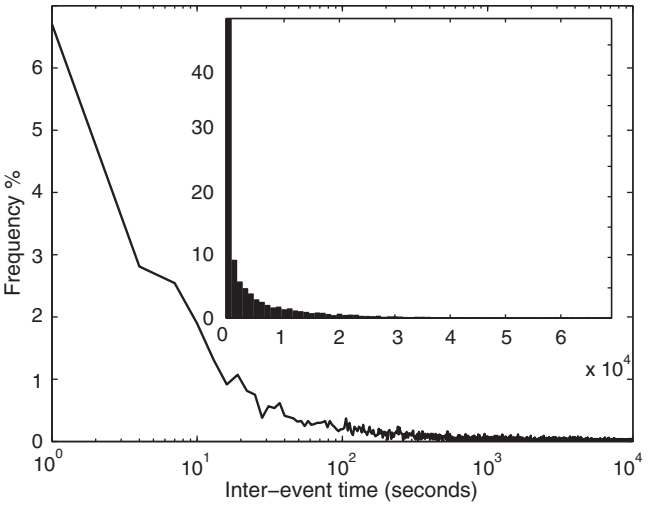

Figure 6. Interevent times for all detected events. Main plot shows events within 3 s bins on a logarithmic scale, inset has a bin size of 1000 s and uses a linear scale. Interevent times peak between 0 and 3 s, with 27% of all detections having interevent times less than 100 s.

2.3. Event Verification

To determine an appropriate MAD multiplier for our detection threshold, we have undertaken synthetic testing following the method of *Rawlinson* [2011]. This involves seeding a day of random noise with copies of real LFE templates at random locations and with random SNRs before applying the same cross-correlation algorithm used in detection.

This testing shows that using a threshold of 8 × MAD will give between 0 and 3 false detections per day per template (mean of 0.2 for days of high noise, such as after large regional earthquakes, and mean of 0.01 for quiet days without large earthquakes) and detect 70–90% of all actual LFEs above a SNR of 0.2, depending on the template and noise conditions. Testing reveals that a complete (100% positive detections) catalog is achieved at approximately SNR=0.8 throughout the time period analyzed. By empirically determining the daily noise levels, we determine an average magnitude of completeness (M_c) of 0.6. This M_c is strongly time varying, however, with fluctuating noise levels resulting in completeness values varying between −0.5 and +2.0 (Figure 5). The implications of this time varying M_c are discussed later.

We do expect a higher false detection rate during the aftershock sequences of large regional earthquakes. However, of the 1400 tests run at 8 × MAD throughout a day of phase-randomized data containing the amplitude information from the Dusky Sound earthquake and its aftershocks, in 1176 (84%) of tests we made 0 false detections and 196 (14%) of tests contained 1 false detection. The maximum false detections per template per day is 3, at a threshold of 8 × MAD. This maximum false detection rate was found in 2 (0.1%) test runs through high-noise conditions. For further details of the synthetic testing, see the Supporting information.

3. Observations

The 14 LFE families in our catalog occur within a cross-sectional area of ∼ 21 × 36 km and depth extent of 15 km, taking into account the uncertainties in locations in *NonLinLoc* [*Lomax et al*., 2000]. The hypocentres appear anticorrelated in depth with "typical" seismicity, lying beneath the seismogenic zone (0–12 km, *Boese et al*. [2012]). Twelve of the 14 families lie on or near the Alpine Fault inferred from GPS measurements [*Lamb and Smith*, 2013], coincident with deep reflectors [*Okaya et al*., 2007] within a zone of low seismic velocities [*Smith et al*., 1995; *Stern et al*., 2001] and high P-wave attenuation (low Qp) [*Eberhart-Phillips et al*., 2008] (Figure 3). The other two families appear to be separated from the main cluster of families and lie to the south-west of the inferred Alpine Fault. LFEs also occur at markedly shallower depths than deep subcrustal earthquakes [*Boese et al*., 2013], suggesting a different process of seismogenesis.

LFEs are ubiquitous throughout the record, occurring at a relatively constant long term rate of 8.5 per day (Figure 5), rather than being confined to tremor periods. They are nevertheless clustered, with 50% of detections having interevent times of less than 1000 s, and 11% having interevent times less than 8 s (Figure 6). The clustering of interevent times close to 0 s is typical of LFE swarms coinciding with tremor periods identified by *Wech et al*. [2012] and with newly identified tremor periods verified here by eye and found to be located near the LFE source region using the WECC method [*Wech*, 2010] (Figure 4).

Tremor periods previously identified by *Wech et al*. [2012] correspond to abrupt increases in LFE detection rates (Figures 4 and 7). We are able to identify all but three of the 19 tremor bursts *Wech et al*. [2012]

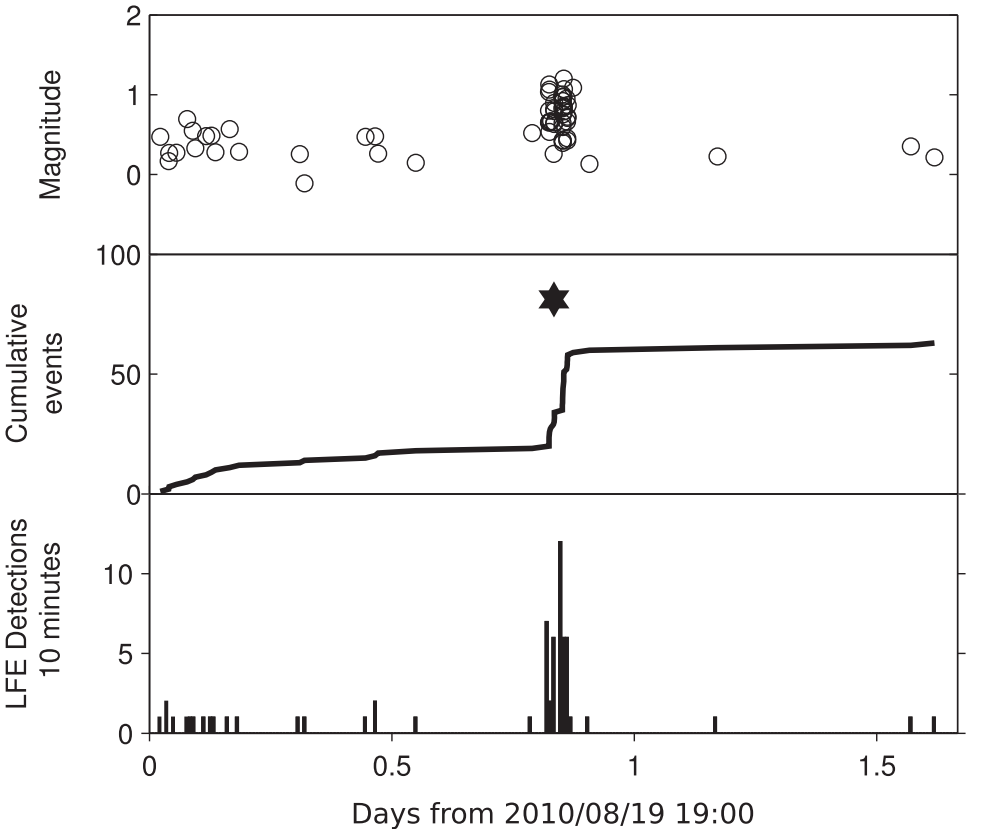

Figure 7. LFE detections for a representative tremor period (onset marked by black star) previously detected by *Wech et al.* [2012] at UTC 20 August 2010, 04:46–05:57. (top) LFE magnitudes with time, (middle) cumulative LFE detections, and (bottom) LFE detections per hour. Tremor periods observed through LFE detection display a sharp spike in LFE detections at tremor onset (5–15 detections per 10 min) without major variation in magnitudes or change in background detection rate.

recognized, reinforcing the idea of tremor being composed of LFE swarms. LFEs account for roughly 12–24% of the previously detected tremor, depending on whether phase delays due to traveltimes are included or not. This estimate does not include the effects of scattering or multiples and should be considered a minimum value. Two of the three tremor periods not identified here were located at least 15 km from our template locations and at least 10 km from the nearest detecting station. One location for tremor not detected by LFEs, however, lies near to the region of LFE detections. For the tremor episode on 3 August 2011, two distinct tremor locations were calculated by *Wech et al.* [2012] within 5 min of each other, one within the LFE source region and one $\sim$ 15 km southwest of the LFEs. We suggest that the tremor location within the LFE source region may be an artifact and the second location (to the southwest) is more likely. Attempts to pick LFEs within these three bursts of tremor have not yet proven fruitful, with fewer than five stations showing detections. An ongoing southern extension of the SAMBA may yield greater template coverage for future studies.

One of the strengths of the iterative cross correlation and stacking method is our ability to identify LFEs within noisy time series, and in particular within aftershock sequences and during the mainshock coda of large regional earthquakes (Figure 8). Following five large regional earthquakes during the study period (Dusky Sound 15 July 2009, M_w7.8 [*Beavan et al.*, 2010]; Darfield (Canterbury) 3 September 2010, M_w7.1 [*Quigley et al.*, 2012]; Christchurch 21 February 2011, M_w6.2 [*Holden*, 2011]; Christchurch 13 June 2011, M_w6.0 [*Holden*, 2011], and Christchurch 23 December 2011 M_w5.9 [*Bannister and Gledhill*, 2012], dates in UTC), we observe distinct increases in LFE rate above the expected increase in false detections (see section 2.3). After each earthquake, we see a decay toward the background rate, but the duration of the decay after each earthquake is different. Reliable magnitude estimation within aftershock sequences remains problematic, with high LFE magnitudes within the aftershock sequences assessed here often corresponding to earthquake contamination.

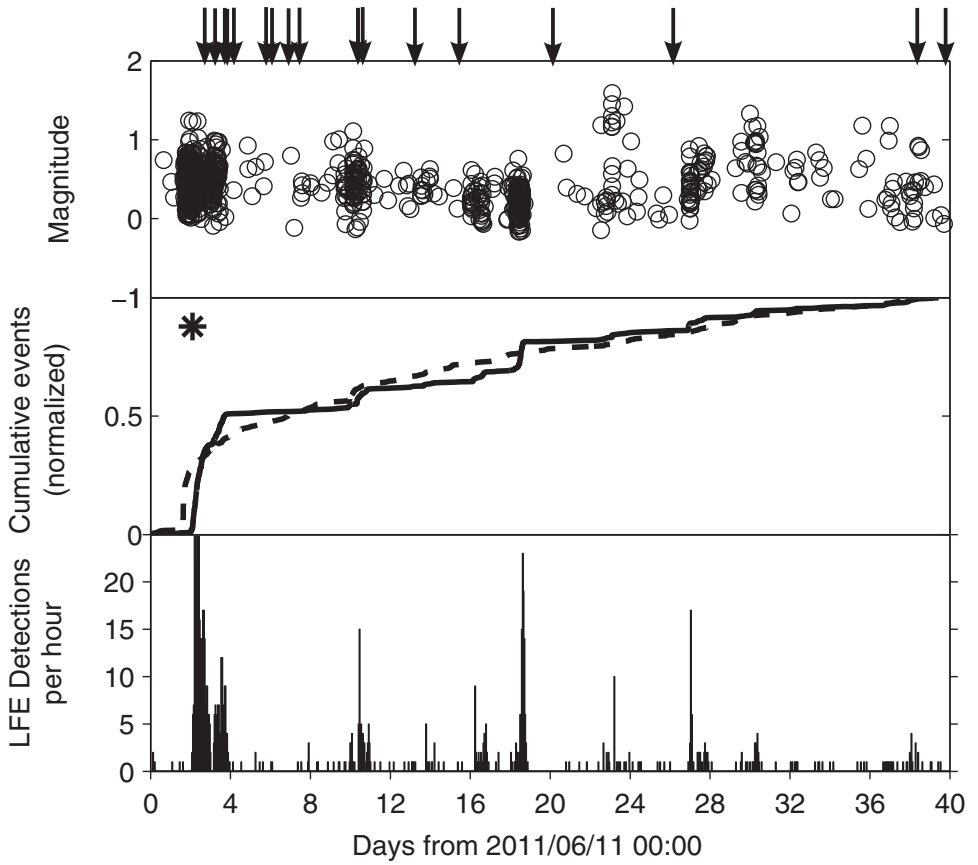

Figure 8. LFEs detected after the June Christchurch earthquake (M_w 6.0 [*Holden*, 2011], UTC 13 June 2011, 02:20 origin time plotted as black asterisk). (top) LFE magnitudes with time, (middle) normalized cumulative detections for both LFEs (solid line) and "typical" $M_w > 3.0$ earthquakes (dashed line), and (bottom) LFE detections per hour. LFE detections after large regional earthquakes show a gradual response with detection rates increasing to 5–15 per hour, a larger range of magnitudes than is seen within tremor, and a steady decrease in rates toward background levels. This decay toward background levels is more staccato than that seen in "typical" earthquake aftershocks (dashed line top), with spikes in detection rate associated with larger aftershocks suggesting triggering by earthquakes of lower magnitudes than the main M_w 6.0 earthquake. Earthquakes $M_w > 4.0$ in the GeoNet catalog covering the whole of South Island are highlighted by black arrows.

Each LFE family analyzed shows a slightly different temporal evolution during known tremor periods and in response to large regional earthquakes (Figure 9). Nevertheless, the range of magnitudes and average magnitudes of each family are quite similar. Family ID:61044 has the largest mean magnitude (M_L 0.9) and highest number of detections (1726; Table 1) suggesting that detection rate and magnitude are correlated; however, this is not the case because, for instance, family ID:37575 has a similarly high number of detections (1456), but a much lower mean magnitude (M_L 0.4). Basic analysis shows no trend in our small dataset between family mean M_L and number of detections. In general, the cumulative detections of each family are quite consistent, with only two families containing more than 1000 events.

The LFEs we have detected do not exhibit a simple Gutenberg-Richter power law scaling, as plots of the logarithm of the cumulative frequency against magnitude (Figure 10) are not well fit by a linear gradient above the M_c. The implications of this are discussed below. However, PGV amplitudes do approximately follow an exponential law for individual LFE families as reported previously by *Shelly and Hardebeck* [2010] for the San Andreas fault. We see evidence for two main forms of this exponential relation, with five families showing similar gradients to family ID:61220 (Figure 10) and the other nine families exhibit a shallower gradient similar to family ID:37575.

For the two LFE families with much higher numbers of detections than average, the majority of events occur closely spaced in time (Figure 9). For family ID:61044, 30% of the 1726 detections were made following the Darfield earthquake. This family showed a muted response to the Dusky Sound earthquake in 2009 but more pronounced responses to the Christchurch earthquakes following the Darfield

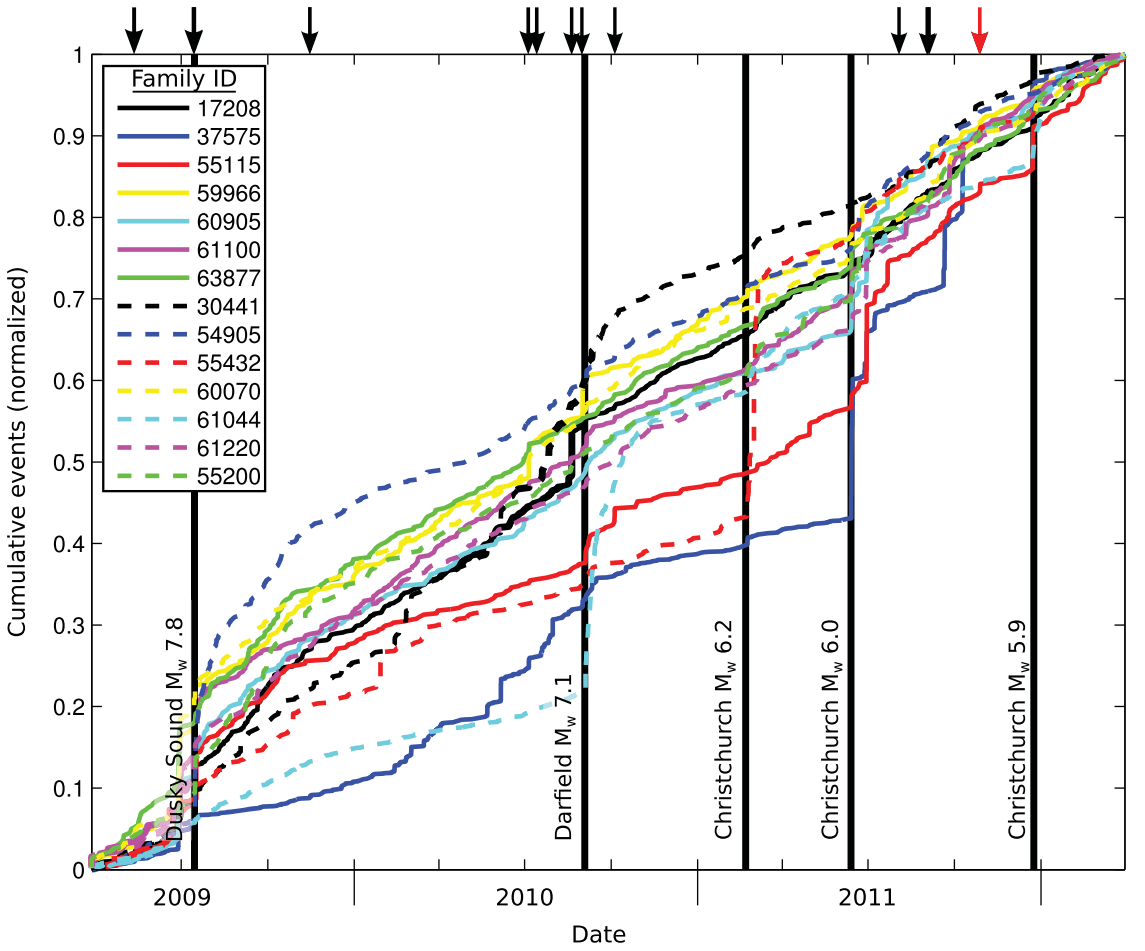

Figure 9. Normalized detections for each family with previously detected tremor events [*Wech et al*., 2012] indicated by arrows and large regional earthquakes seen to elicit an LFE response indicated by solid black vertical lines. Red arrow indicates a newly identified tremor period defined by a spike in LFE generation. Individual families respond differently to different tremor events and earthquakes. Notably, the family with the most detections (Family ID:61044, 1726 detections) responds most strongly to the Darfield earthquake and also shows a strong response to the two Christchurch earthquakes.

earthquake. Family ID:37575 produced nearly 20% of its constituent LFEs within a month of the 13 June 2011 Christchurch earthquake, and shows a marked increase in activity after this earthquake. This family showed a decreased rate of detection after the Darfield earthquake, in contrast to family ID:61044.

LFE detections made within aftershock sequences do not appear to be "typical" aftershocks. Extensive detection testing within synthetic aftershock sequences has shown that although our false detection rate increases, this increase is unable to account for the overall detection rate increases observed. We have also confirmed by manual assessment for a day of data within the aftershocks of the Darfield earthquake that LFE detections are not made at the same time, or crucially, with the same station-delays as aftershocks. Furthermore LFE decay patterns after triggering events do not follow the same aftershock decay pattern as the typical earthquake aftershocks of these events: rather, we observe spikes in LFE detections concurrent with the mainshock and subsequent large events with periods of relative quiescence between (Figure 8).

4. Discussion

4.1. LFE Family Locations

Tremor and LFEs detected at plate boundaries have been interpreted to be the seismic manifestation of slow shear slip [e.g., *Ide et al*., 2007; *Wech and Creager*, 2007; *Shelly*, 2010; *Rubin and Armbruster*, 2013]. In

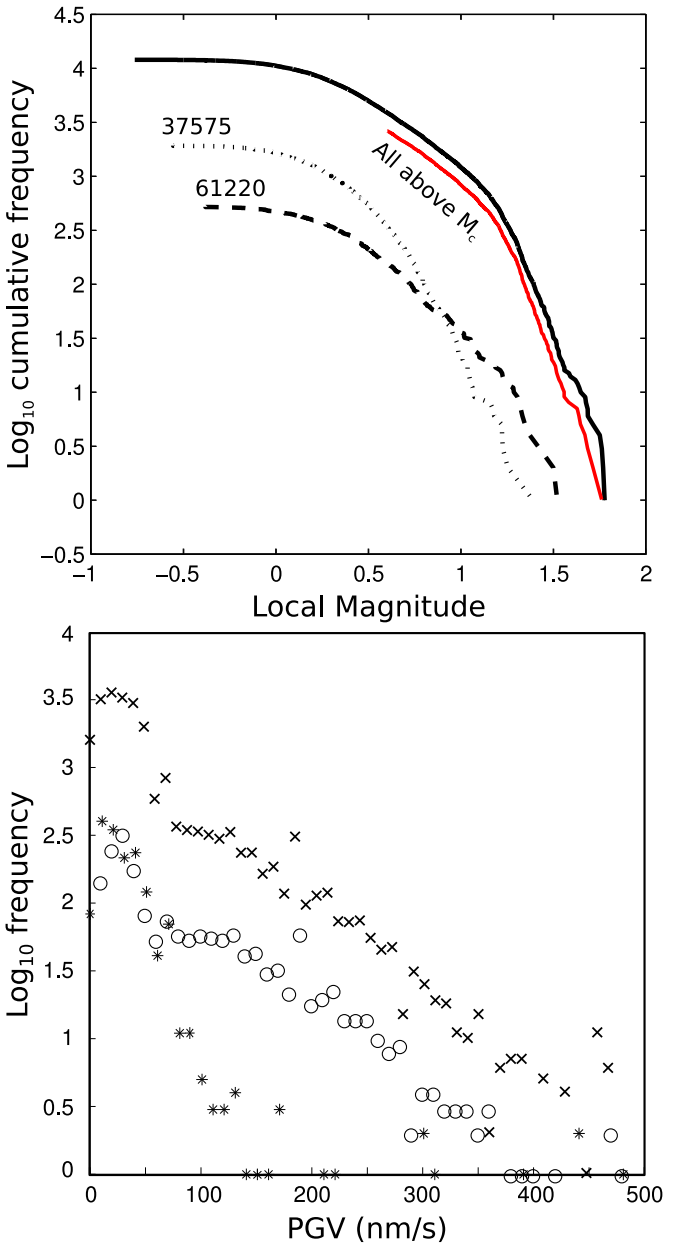

Figure 10. Cumulative frequency-magnitude (top) and frequency-amplitude (PGV) (bottom) relations for all LFEs (solid line and crosses), family ID:37575 (dotted line and stars) and family ID:61220 (dashed line and circles). (top) Red line shows the frequency-magnitude relation for the complete part of the catalog (LFEs with $M_L \geq M_c$ for days with $M_c \leq 0.6$) which follows a similar relationship to the full catalog (black). PGV amplitudes scale approximately linearly with the logarithm of frequency, with each family having a different scaling parameter. Individual family scaling parameters have two dominant forms exemplified by families ID:37575 and ID:61220. The sum of these two forms is evident as a spike in occurrence at low PGV amplitudes in the plot of all LFE detections due to the amplitude relation of families similar to family ID:37575, followed by a change in gradient due to families more similar to family 61220.

this case, the consistency in the locations of LFEs with the location of the deep extent of the Alpine Fault inferred by other means (GPS inversion [*Lamb and Smith*, 2013], seismic reflection [*Okaya et al*., 2007] and velocity models [*Stern et al*., 2001; *Smith et al*., 1995]), and the contemporaneous detection of tremor and LFEs suggests that the LFEs represent slow shear slip on the deep extent of the Alpine Fault. However, without reliable focal mechanisms, and given the small number of LFE families detected to date, we cannot yet unequivocally relate the LFEs detected in this study to shear slip. We are hopeful that the improved azimuthal coverage provided by the recent southern SAMBA extension (stations SOLU and MTBA in Figure 1) and ongoing research into seismic velocity structure beneath the Southern Alps will improve LFE location uncertainties, particularly in depth, and enable focal mechanism parameters to be evaluated in the future.

We hypothesize that these LFEs are generated on asperities within an otherwise aseismic, creeping region of the Alpine Fault, following the model of *Ide* [2008]. Due to low SNR values of the LFEs, and corresponding low single-channel correlations (average 0.5), we have not yet been able to reliably relocate the LFEs within individual families. However, because we do not detect the same event with more than one template, we infer that the scatter of hypocentres within an individual LFE family is smaller than the average distance between different families.

Twelve of the 14 LFE locations in this region are clustered in space, near the inferred change in dip from a steep (45–60°) stably sliding fault updip of the LFE generation region, to a shallower dip (15–20°) partially locked zone [*Lamb and Smith*, 2013]. We hypothesize that this transition allows for near-constant slip while

having enough asperities to generate LFEs. The remaining two locations may be indicative of a more steeply dipping strand of the Alpine Fault as discussed by *Norris and Toy* [2014], but further events are required to substantiate this.

Some tremor depths estimated by *Wech et al*. [2012] exceed those of the LFEs reported here. It is possible our analysis misses deep tremor due to low SNR values, but during all deep tremor periods identified by *Wech et al*. [2012] we see active LFE generation at shallower levels. We thus suggest that the discrepancies in estimates of depths reflect the large uncertainties due to tremor-source geometry and network limitations *Wech et al*. [2012] pointed out.

Tremor and LFEs are often interpreted to be associated with fluids, either in relation to fluid migration or high fluid pressure resulting in reduced normal stress and allowing for shear slip [e.g., *Shelly et al*., 2006; *Thomas et al*., 2009; *Bostock et al*., 2012; *Wech et al*., 2012]. If the LFEs documented here do indicate deep slip on the Alpine fault as we hypothesize, then the low Q_p and low seismic velocity that characterize the source region (Figure 3) may in some manner be associated with fault weakening. *Eberhart-Phillips et al*. [2008] interpreted the region of low Q_p here to be the downdip extension of the Alpine Fault beneath South Island, and the high attenuation itself to mark the presence of metamorphic fluids. This is compatible with the interpretation of *Stern et al*. [2001] who concluded that the low seismic velocities correspond to increased fluid pressures and associated fault weakness.

The 14 LFE templates and their subsequent detections are unlikely to represent all the tremor on the Alpine Fault in this region; instead they represent the strongest LFE signals detected with a suboptimal seismic network. The recent extension of SAMBA southward should allow future studies of LFEs and tremor to be made with lower magnitudes of completeness, greater spatial coverage and improved hypocentral resolution.

As noted by other authors [e.g., *Boese et al*., 2012; *Wech et al*., 2012; *Boese et al*., 2013], there is a distinct change in the pattern of seismicity along strike on the Alpine Fault. Of particular relevance to this study is the lack of LFE detections north-east of Mt. Cook. This change is coincident with the abrupt change in shallow seismicity noted by *Boese et al*. [2012] and in deep seismicity [*Boese et al*., 2013] (Figure 3). However, as we have only looked for LFE templates within known tremor periods, also seen to locate south-west of Mt. Cook, the lack of LFE locations away from tremor locations is unsurprising. We therefore cannot rule out LFE generation north-east of the current LFE source region, but suggest that if LFEs are generated to the north-east they do not generate tremor as demonstrated by *Wech et al*. [2012].

Seismic [e.g., *Okaya et al*., 2007] and geological [e.g., *Little et al*., 2005] evidence suggests that the geometry of the Alpine Fault changes in the region beneath Mt. Cook from a listric fault south of Mt. Cook to a near-vertical structure in the north. This change in geometry may be associated with the termination of a partially subducted remnant passive margin attached to the Australian plate and extending south-westward beneath the plate boundary [*Sutherland et al*., 2000]. *Boese et al*. [2013] considered that the partially subducted remnant passive margin may explain the transition in deep seismicity beneath South Island. The similarity in termination points for deep earthquakes, tremor generating LFEs, and the proposed remnant passive margin suggests a common control.

4.2. Interevent Timing and Magnitudes

We observe tremor beneath the central Southern Alps to be a superposition of multiple LFEs occurring with small interevent times in a swarm-like manner, as demonstrated by *Shelly et al*. [2007]. However, a large portion of the catalog presented here exhibits discrete behavior, with large interevent times that are not tremor-like. As our catalog is largely composed of events near or at the limit of our detection and outside our network (Figure 3), we cannot be certain that those discrete events within the catalog are not related to smaller events, or events outside our detection region.

Our observations of near-constant LFE generation rate suggest that LFEs represent quasi-continuous punctuated creep on the deep extent of the Alpine Fault, and provide the first evidence of such slip on the deep extent of the Alpine Fault. With magnitudes apparently at or near our detection threshold (M_c0.6) and deep hypocentres, the lack of geodetically detectable slow slip is unsurprising. Detection of slow slip is also hindered by the constancy of LFE generation and hence slow slip, with brief swarms (tremor events) lasting 5–120 min suggesting similarly brief slip rate increases. Abrupt LFE detection rate increases coincident with large regional earthquakes may be indicative of triggering by transient or static stress shifts [*Boese et al*.,

2014]. A full investigation of LFE triggering characteristics in the Southern Alps is the subject of ongoing research and beyond the scope of this paper. However, initial analysis of the apparently triggered LFE rate increases shows that LFE decay rates following regional earthquakes do not follow the same decay pattern as "typical" aftershocks generated in the brittle crust by the same events.

We are not aware of LFE catalog completeness being computed before. *Shelly and Hardebeck* [2010] provided some indication of completeness by demonstrating the level at which LFE size stops following an exponential law, but this approach requires the assumption that LFEs follow an exponential law. Rather than imposing this condition (or indeed assuming a G-R law), we have estimated the completeness empirically based on the SNR values required for 100% detections in synthetic testing (section 2.3). Analysis of the magnitude-frequency characteristics above this level shows no relationship between magnitude and recurrence interval. This is again likely to be a characteristic of our swarm-dominated catalog.

The fact that M_c varies from day to day does not preclude analysis of the frequency-magnitude characteristics of the LFE dataset as a whole. Events of $M_L \geq 0.6$ occurring on the subset of days for days on which $M_c \leq 0.6$ exhibit the same frequency-magnitude characteristics as the full catalog (Figure 10). If LFEs scaled in a similar fashion to "typical" repeating earthquakes, we might expect a linear relationship between the logarithm of cumulative frequency and magnitude, but this is not the case. Rather, individual families are well-fit by an exponential model above M_c and below a maximum magnitude value. This maximum magnitude may be an indication of the limit of fault (asperity) size as identified on a global scale for "typical" earthquakes by *Kagan* [2002].

The approximately exponential distribution of LFE amplitudes seen here is consistent with the San Andreas LFE amplitude distributions shown by *Shelly and Hardebeck* [2010], albeit here at much higher amplitudes, and with the observations of *Watanabe et al.* [2007] of amplitude-duration distributions in nonvolcanic tremor. This exponential distribution is also consistent with tremor amplitude-duration characteristics in volcanic settings [e.g., *Benoit et al*., 2003]. Such an exponential relationship in tremor implies that the source has a characteristic scale. In volcanic settings, this can be attributed to constraints imparted by the magmatic plumbing system [e.g., *Aki and Koyanagi*, 1981; *Benoit et al*., 2003]. *Watanabe et al*. [2007] argued that a characteristic length scale for the nonvolcanic tremor source process, possibly the length of fluid-filled cracks, is required to describe the exponential relationship found in tremor properties in southwest Japan.

The source process for nonvolcanic tremor and LFEs remains poorly understood. The exponential frequency-magnitude relationships seen here may be related to a characteristic length scale for individual LFE families. This characteristic length scale is likely to be related to the asperity size, the limit of which may be inferred from the cut-off magnitude. If this is the case, then LFE magnitude could be used to directly monitor the amount of slip at the deep extent of faults. However, the frequency-magnitude characteristics could also be related to some process required to slow earthquake rupture in the generation of these "slow" earthquakes [*Kaproth and Marone*, 2013], related to the damping term described by *Ide* [2008].

5. Conclusions

We have presented the first evidence of LFEs associated with the Alpine Fault in New Zealand's South Island. Our results demonstrate that tremor occurring on or near the Alpine Fault is composed of LFE swarms, but that LFEs also occur quasi-continuously without generating extended-duration tremor. LFEs in our catalog exhibit a range of interevent times dominated by short interevent times coincident with swarms (tremor) while also containing many temporally isolated events. We interpret that these discrete events indicate that the deep extent of the Alpine Fault is undergoing quasi-continuous creep punctuated by rate increases manifesting as tremor.

We have located 14 LFE families and found that 12 of these 14 families lie within $\sim$ 10 km of the Alpine Fault inferred from GPS measurements [*Lamb and Smith*, 2013], within an area of high seismic reflectivity [*Okaya et al*., 2007], anticorrelated in depth with both shallow [*Boese et al*., 2012] and deep [*Boese et al*., 2013] seismicity in the region. We conclude that LFEs (and therefore tremor) in the Southern Alps are the manifestation of slow shear slip on the plate interface. Furthermore, 12 of 14 LFE families lie within a zone of low Q_p which we interpret to be a sign of fluid-weakened rock, thereby allowing for ongoing slow slip on an otherwise locked region of the Alpine Fault. We suggest that these fluids may be generated as the

products of metamorphism of a partially subducted passive margin which terminates beneath Mt. Cook. This also may explain the lack of LFEs and tremor north-east along strike from our LFE families.

The LFE magnitudes we compute do not scale according to a power law, but instead appear to scale according to an exponential law suggestive of a characteristic length scale in LFE source generation. We interpret this to be indicative of constant slip patch sizes for individual LFE families associated with the size of asperities upon which LFEs nucleate in an otherwise stably sliding region of the Alpine Fault.

Further study using data from the forthcoming SAMBA extension south of the current LFE source region will further constrain the extent of LFE generation and lead to a more representative view of slip occurring at depth on the Alpine Fault.

Acknowledgments

We are grateful to Carolin Boese and Aaron Wech for ongoing guidance relating to this work, and for permission to use their results. We thank Euan Smith and Katrina Jacobs for stimulating discussions, and Roland Burgmann and one anonymous reviewer for helpful comments that improved this manuscript. C. Chamberlain is supported by Victoria University of Wellington. This work was funded by the Marsden Fund of the Royal Society of New Zealand. J. Townend acknowledges the support of Fulbright New Zealand and Stanford University during this project.

References

Aki, K., and R. Koyanagi (1981), Deep volcanic tremor and magma ascent mechanism under Kilauea, Hawaii, *J. Geophys. Res.*, *86*(B8), 7095–7109, doi:10.1029/JB086iB08p07095.

Bannister, S., and K. Gledhill (2012), Evolution of the 2010–2012 Canterbury earthquake sequence, *New Zeal. J. Geol. Geophys.*, *55*(3), 295–304, doi:10.1080/00288306.2012.680475.

Beavan, J., P. Tregoning, and M. Bevis (2002), Motion and rigidity of the Pacific Plate and implications for plate boundary deformation, *J. Geophys. Res.*, *107*(B10), 2261, doi:10.1029/2001JB000282.

Beavan, J., S. Samsonov, P. Denys, R. Sutherland, N. Palmer, and M. Denham (2010), Oblique slip on the Puysegur subduction interface in the 2009 July MW 7.8 Dusky Sound earthquake from GPS and InSAR observations: Implications for the tectonics of southwestern New Zealand, *Geophys. J. Int.*, *183*(3), 1265–1286, doi:10.1111/j.1365-246X.2010.04798.x.

Benoit, J., S. McNutt, and V. Barboza (2003), Duration amplitude distribution of volcanic tremor, *J. Geophys. Res.*, *108*(B3), 2146, doi:10.1029/2001JB001520.

Berryman, K. R., U. A. Cochran, K. J. Clark, G. P. Biasi, R. M. Langridge, and P. Villamor (2012), Major earthquakes occur regularly on an isolated plate boundary fault, *Science*, *336*(6089), 1690–1693, doi:10.1126/science.1218959.

Boese, C. (2012), Microseismicity in the central Southern Alps, Westland, New Zealand, PhD thesis, Victoria Univ. of Wellington, Wellington, New Zealand.

Boese, C., T. Stern, and J. Townend (2013), Sub-crustal earthquakes within the Australia Pacific plate boundary zone beneath the Southern Alps, New Zealand, *Earth Planet. Sci. Lett.*, *376*, 212–219.

Boese, C. M., J. Townend, E. Smith, and T. Stern (2012), Microseismicity and stress in the vicinity of the Alpine Fault, central Southern Alps, New Zealand, *J. Geophys. Res.*, *117*, B02302, doi:10.1029/2011JB008460.

Boese, C. M., K. M. Jacobs, E. G. C. Smith, T. A. Stern, and J. Townend (2014), Background and delayed-triggered swarms in the central Southern Alps, South Island, New Zealand, *Geochem., Geophys., Geosys.*, *15*, 945–964, doi:10.1002/2013GC005171.

Bostock, M. G., A. A. Royer, E. H. Hearn, and S. M. Peacock (2012), Low frequency earthquakes below southern Vancouver Island, *Geochem. Geophys. Geosyst.*, *13*, Q11007, doi:10.1029/2012GC004391.

Brown, J. R., G. C. Beroza, and D. R. Shelly (2008), An autocorrelation method to detect low frequency earthquakes within tremor, *Geophys. Res. Lett.*, *35*, L16305, doi:10.1029/2008GL034560.

Brown, J. R., S. G. Prejean, G. C. Beroza, J. S. Gomberg, and P. J. Haeussler (2013), Deep low-frequency earthquakes in tectonic tremor along the Alaska-Aleutian subduction zone, *J. Geophys. Res. Solid Earth*, *118*, 1079–1090, doi:10.1029/2012JB009459.

Cox, S., and R. Sutherland (2013), Regional geological framework of South Island, New Zealand, and its significance for understanding the active plate boundary, in *A Continental Plate Boundary: Tectonics at South Island, New Zealand*, edited by D. Okaya, T. Stern, and F. Davey, pp. 19–46, AGU, Washington, D. C.

Eberhart-Phillips, D., M. Chadwick, and S. Bannister (2008), Three-dimensional attenuation structure of central and southern South Island, New Zealand, from local earthquakes, *J. Geophys. Res.*, *113*, B05308, doi:10.1029/2007JB005359.

Frank, W. B., N. M. Shapiro, V. Kostoglodov, A. L. Husker, M. Campillo, J. S. Payero, and G. A. Prieto (2013), Low-frequency earthquakes in the Mexican Sweet Spot, *Geophys. Res. Lett.*, *40*, 2661–2666, doi:10.1002/grl.50561.

Fry, B., K. Chao, S. Bannister, Z. Peng, and L. Wallace (2011), Deep tremor in New Zealand triggered by the 2010 Mw8.8 Chile earthquake, *Geophys. Res. Lett.*, *38*, L15306, doi:10.1029/2011GL048319.

Havskov, J. and L. Ottemöller (2010), *Routine Data Processing in Earthquake Seismology*, pp. 154–160, Springer, Dordrecht, doi:10.1007/978-90-481-8697-6.

Holden, C. (2011), Kinematic Source Model of the 22 February 2011 Mw 6.2 Christchurch Earthquake Using Strong Motion Data, *Seismol. Res. Lett.*, *82*(6), 783–788, doi:10.1785/gssrl.82.6.783.

Houlié, N., and T. Stern (2012), A comparison of GPS solutions for strain and SKS fast directions: Implications for modes of shear in the mantle of a plate boundary zone, *Earth Planet. Sci. Lett.*, *345–348*, 117–125, doi:10.1016/j.epsl.2012.06.029.

Ide, S. (2008), A Brownian walk model for slow earthquakes, *Geophys. Res. Lett.*, *34*, L17301, doi:10.1029/2008GL034821.

Ide, S., D. R. Shelly, and G. C. Beroza (2007), Mechanism of deep low frequency earthquakes: Further evidence that deep non-volcanic tremor is generated by shear slip on the plate interface, *Geophys. Res. Lett.*, *34*, L03308, doi:10.1029/2006GL028890.

Kagan, Y. K. (2002), Seismic moment distribution revisited: I. Statistical results, *Geophys. J. Int.*, *148*, 520–541.

Kaproth, M., and C. Marone (2013), Slow earthquakes, preseismic velocity changes, and the origin of slow frictional stick-slip, *Science*, *341*, 1229–1232, doi:10.1126/science.1239577.

Lamb, S., and E. Smith (2013), The nature of the plate interface and driving force of interseismic deformation in the New Zealand plate-boundary zone, revealed by the continuous GPS velocity field, *J. Geophys. Res. Solid Earth*, *118*, 3160–3189, doi:10.1002/jgrb.50221.

Little, T., R. Wightman, R. Holcombe, and M. Hill (2007), Transpression models and ductile deformation of the lower crust of the Pacific Plate in the central Southern Alps, a perspective from structural geology, in *A Continental Plate Boundary: Tectonics at South Island, New Zealand*, edited by D. Okaya, T. Stern, and F. Davey, pp. 273–290, AGU, Washington, D. C.

Little, T. A., S. Cox, J. K. Vry, and G. Batt (2005), Variations in exhumation level and uplift rate along the obliqu-slip Alpine fault, central Southern Alps, New Zealand, *Geol. Soc. Am. Bull.*, *117*(5), 707–723, doi:10.1130/B25500.1.

Lomax, A., J. Virieux, P. Volant, and C. Berge (2000), Probabilistic earthquake location in 3D and layered models: Introduction of a Metropolis-Gibbs method and comparison with linear locations, in *Advances in Seismic Event Location*, edited by C. Thurber and N. Rabinowitz, pp. 101–134, Kluwer Acad., Amsterdam.

Nadeau, R. M., and D. Dolenc (2005), Nonvolcanic tremors deep beneath the San Andreas Fault, *Science*, *307*, 389, doi:10.1126/science.1107142.

Norris, R. J., and A. F. Cooper (2000), Late quaternary slip rates and slip partitioning on the Alpine Fault, New Zealand, *J. Struct. Geol.*, *23*, 507–520.

Norris, R. J., and V. G. Toy (2014), Continental transforms: A view from the Alpine Fault, *J. Struct. Geol.*, *64*, 3–31, doi:10.1016/j.jsg.2014.03.003.

Obara, K. (2002), Nonvolcanic deep tremor associated with subduction in southwest Japan, *Science*, *296*(5573), 1679–1681.

Okaya, D., T. Stern, and F. Davey (Eds.) (2007), *A Continental Plate Boundary: Tectonics at South Island, New Zealand, Geophys. Monogr. Ser. 175*, pp. 47–72, AGU, Washington, D. C., doi:10.1029/GM175.

O'Keefe, B. C. (2008), Microseismicity of the Central Alpine Fault Region, New Zealand by, MSc thesis, Victoria Univ. of Wellington, Wellington, New Zealand.

Peng, Z., J. E. Vidale, A. G. Wech, R. M. Nadeau, and K. C. Creager (2009), Remote triggering of tremor along the San Andreas Fault in central California, *J. Geophys. Res.*, *114*, B00A06, doi:10.1029/2008JB006049.

Quigley, M., R. V. Dissen, and N. Litchfield (2012), Surface rupture during the 2010 Mw 7.1 Darfield (Canterbury) earthquake: Implications for fault rupture dynamics and seismic-hazard analysis, *Geology*, *40*, 55–58.

Rawlinson, Z. (2011), Microseismicity associated with actively exploited geothermal systems: Earthquake detection and probabilistic location at Rotokawa and statistical seismic network design at Kawerau, MSc thesis, Victoria Univ. of Wellington, Wellington, New Zealand.

Rogers, G., and H. Dragert (2003), Episodic tremor and slip on the Cascadia subduction zone: The chatter of silent slip, *Science*, *300*(5627), 1942–1943.

Royer, A. A., and M. G. Bostock (2013), A comparative study of low frequency earthquake templates in northern Cascadia, *Earth Planet. Sci. Lett.*, doi:10.1016/j.epsl.2013.08.040, in press.

Rubin, A., and J. Armbruster (2013), Imaging slow slip fronts in Cascadia with high precision crossstation tremor locations, *Geochem. Geophys. Geosys.*, *14*, 5371–5392, doi:10.1002/2013GC005031.

Shelly, D., G. Beroza, S. Ide, and S. Nakamula (2006), Low-frequency earthquakes in Shikoku, Japan, and their relationship to episodic tremor and slip., *Nature*, *442*(7099), 188–191, doi:10.1038/nature04931.

Shelly, D. R. (2010), Migrating tremors illuminate complex deformation beneath the seismogenic San Andreas fault, *Nature*, *463*(7281), 648–652, doi:10.1038/nature08755.

Shelly, D. R., and J. L. Hardebeck (2010), Precise tremor source locations and amplitude variations along the lower-crustal central San Andreas Fault, *Geophys. Res. Lett.*, *37*, L14301, doi:10.1029/2010GL043672.

Shelly, D. R., G. C. Beroza, and S. Ide (2007), Non-volcanic tremor and low-frequency earthquake swarms, *Nature*, *446*(7133), 305–307, doi:10.1038/nature05666.

Smith, E., T. Stern, and B. O'Brien (1995), A seismic velocity profile across the central South Island, New Zealand, from explosion data, *New Zeal. J. Geol. Geophys.*, *38*, 565–570.

Stern, T., S. Kleffmann, and D. Okaya (2001), Low seismic-wave speeds and enhanced fluid pressure beneath the Southern Alps of New Zealand, *Geology*, *29*, 679–682, doi:10.1130/0091-7613(2001)029¡0679.

Sutherland, R., F. Davey, and J. Beavan (2000), Plate boundary deformation in South Island, New Zealand, is related to inherited lithospheric structure, *Earth Planet. Sci. Lett.*, *177*(3-4), 141–151, doi:10.1016/S0012-821X(00)00043-1.

Sutherland, R., K. Berryman, and R. Norris (2006), Quaternary slip rate and geomorphology of the Alpine fault: Implications for kinematics and seismic hazard in southwest New Zealand, *Geol. Soc. Am. Bull.*, *118*(3-4), 464–474, doi:10.1130/B25627.1.

Sutherland, R., et al. (2007), Do great earthquakes occur on the Alpine fault in central South Island, New Zealand?, in *A Continental Plate Boundary: Tectonics at South Island, New Zealand*, edited by D. Okaya, T. Stern and F. Davey, pp. 235–251, AGU, Washington, D. C., doi:10.1029/GM175.

Sutherland, R., et al. (2012), Drilling reveals fluid control on architecture and rupture of the Alpine fault, New Zealand, *Geology*, *40*(12), 1143–1146, doi:10.1130/G33614.1.

Thomas, A. M., R. M. Nadeau, and R. Bürgmann (2009), Tremor-tide correlations and near-lithostatic pore pressure on the deep San Andreas fault, *Nature*, *462*(7276), 1048–51, doi:10.1038/nature08654.

Watanabe, T., Y. Hiramatsu, and K. Obara (2007), Scaling relationship between the duration and the amplitude of non-volcanic deep low-frequency tremors, *Geophys. Res. Lett.*, *34*, L07305, doi:10.1029/2007GL029391.

Wech, A. (2010), Interactive tremor monitoring, *Seismol. Res. Lett.*, *81*(4), 664–669, doi:10.1785/gssrl.

Wech, A., A. Sheehan, C. Boese, J. Townend, T. Stern, and J. Collins (2013), Tectonic Tremor Recorded by Ocean Bottom Seismometers, *Seismol. Res. Lett.*, *84*(5), 752–758.

Wech, A. G., and K. C. Creager (2007), Cascadia tremor polarization evidence for plate interface slip, *Geophys. Res. Lett.*, *34*, L22306, doi:10.1029/2007GL031167.

Wech, A. G., and K. C. Creager (2008), Automated detection and location of Cascadia tremor, *Geophys. Res. Lett.*, *35*, L20302, doi:10.1029/2008GL035458.

Wech, A. G., and K. C. Creager (2011), A continuum of stress, strength and slip in the Cascadia subduction zone, *Nat. Geosci.*, *4*(9), 624–628, doi:10.1038/ngeo1215.

Wech, A. G., C. M. Boese, T. A. Stern, and J. Townend (2012), Tectonic tremor and deep slow slip on the Alpine Fault, *Geophys. Res. Lett.*, *39*, L10303, doi:10.1029/2012GL051751.